Development of an effective modeling method for the mechanical analysis of three-core submarine power cables under tension

Fang, Pan; Li, Xiao; Jiang, Xiaoli; Hopman, Hans; Bai, Yong

DOI
10.1016/j.engstruct.2024.118632

Publication date
2024

Document Version
Final published version

Published in
Engineering Structures

Engineering Structures 317 (2024) 118632

Contents lists available at ScienceDirect

Engineering Structures

journal homepage: www.elsevier.com/locate/engstruct

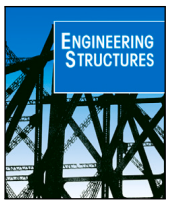

Development of an effective modeling method for the mechanical analysis of three-core submarine power cables under tension

Pan Fang [a,*], Xiao Li [b], Xiaoli Jiang [a], Hans Hopman [a], Yong Bai [c]

[a] Department of Maritime and Transport Technology, Delft University of Technology, Netherlands
[b] Institute of High Performance Computing (IHPC), Agency for Science, Technology and Research (A*STAR), 1 Fusionopolis Way, #16-16 Connexis, Singapore 138632, Republic of Singapore
[c] College of Civil Engineering and Architecture, Zhejiang University, Hangzhou, Zhejiang, PR China

ARTICLE INFO

Keywords:
Periodical boundary conditions
Homogenization
Helical shapes
Tension
Submarine power cables

ABSTRACT

The structural complexity of submarine power cables (SPCs) presents significant challenges in their local mechanical analysis. This paper introduces an advanced modeling method developed for analyzing the mechanical behavior of SPCs under tension, emphasizing both accuracy and efficiency. The method's accuracy is validated through a comparison of simulation results with tension tests conducted on a three-core SPC sample. Efficiency is demonstrated by the superior calculation speed of our model relative to traditional full-scale models. This improved performance is achieved by adopting periodic boundary conditions derived from the homogenization method applied to slender beam-like structures, and by employing a specialized combination of elements to model the helical metal components within the SPCs. The resulting model provides robust capabilities for the mechanical analysis of SPCs under tension and demonstrates significant possibility in accommodating various other loadings.

1. Introduction

Submarine power cables (SPCs) are critical for transmitting electricity from offshore wind farms, which have evolved significantly over the years [1]. As these wind farms expand into more remote and deeper ocean areas to harness richer wind resources, floating platforms have become more prevalent, from which SPCs are suspended, as depicted in Fig. 1. This type of SPC is called dynamic power cable (DPC), as these platforms are subject to constant motion due to waves and currents, subjecting the SPCs to dynamic loadings. Fatigue failure has been reported to be a big concern for the DPCs [2–4].

Unlike static power cables, DPCs constantly suffer from repetitive loadings (tension, bending, and their combination are dominant) during operation due to the movement of floating platforms and environmental loadings resulting from currents and waves [3,4]. The wind industry has considered the fatigue of DPCs to be a great concern and is calling for more research to solve this problem [5–7]. The fatigue analysis is a topic containing several steps and requires engineers from different research fields. Typically, the fatigue analysis for DPCs is classified as global analysis, local analysis and fatigue life prediction [5]. The local analysis acts as a bridge between global analysis and fatigue life prediction, for it not only provides stiffness as input into the global analysis but also transfers the loads from the global analysis into the detailed local behaviors, which will then be used in the fatigue life prediction. The methods for global analysis and fatigue prediction in the wind industry for DPCs are quite similar to those for other traditional flexible structures in the oil and gas industry, as all these structures are regarded as a slender beam in the global study [3,4]. However, due to the differences in the local structure configuration, the local analysis of DPCs can differ from case to case. The accuracy of the local mechanical behaviors from local analysis ultimately determines the fatigue life evaluation to a large extent. CIGRE [5] has shown by a simple example that a minor variation of the predicted stress greatly impacts fatigue life prediction.

Therefore, a more accurate estimation of the local mechanical behaviors of SPCs is required to eliminate the uncertainties as much as possible. Several European projects from the wind industry, WIND EUROPE [8], CARBON TRUST [2,9] and ETIPWind [10] for instance, are calling for the study of DPCs. CARBON TRUST [2,9] and ETIPWind [10] specifically made it clear that design tools are needed for the local mechanical study of DPCs so that the black box is unfolded in front of cable engineers. However, the local mechanical analysis of DPC is still a challenge mainly due to the complicated structure configuration, as shown in Fig. 2(a).

* Corresponding author.
E-mail addresses: P.Fang-1@tudelft.nl (P. Fang), li_xiao@ihpc.a-star.edu.sg (X. Li).

https://doi.org/10.1016/j.engstruct.2024.118632
Received 19 April 2024; Received in revised form 5 July 2024; Accepted 14 July 2024
Available online 23 July 2024

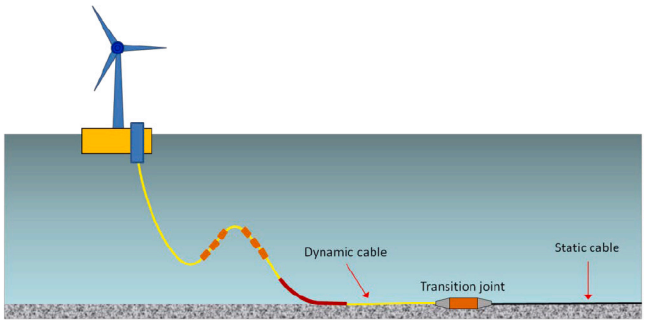

Fig. 1. Facilities in floating wind system [11].

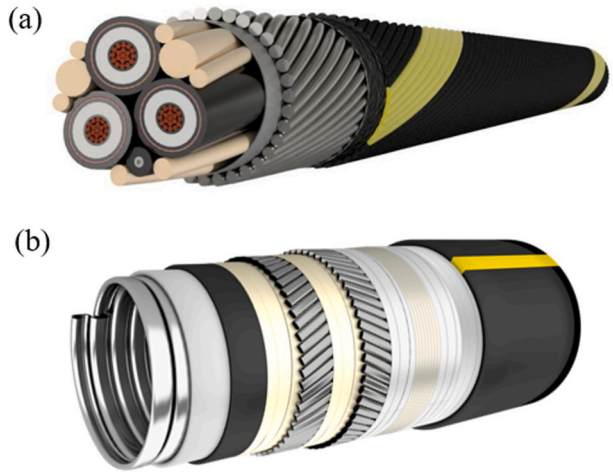

Fig. 2. An SPC (a) [12] and a flexible pipe (b) [13].

During the design of DPCs, both strength and flexibility are major concerns [1] from the mechanical perspective. The strength can be satisfied by adding sufficient metals within the DPC, while the flexibility can be met by designing some of the inner components into helical shape [7]. The helical components aim to release the built-up stress during the loading process by allowing the components to slip away from each other. This design prolongs cable life but also makes it more complicated and not directly comparable to typical flexible structures used in the oil and gas industry [2], such as the flexible pipe shown in Fig. 2(b) where the middle components are absent. Guidelines and standards have emerged for SPCs in recent years to increase safety and reduce uncertainties. Notably, DNV, IEC and CIGRE [5,6,14,15] stand as the preeminent beacons of the SPC standards.

CIGRE [5] presented the details about obtaining the local mechanical behavior of SPCs by test methods. Although the test method is regarded as the most fundamental and reliable, there are at least two limitations.

1. During the preliminary design, a cable sample is unavailable; thus, a test cannot be performed.

2. These tests usually aim to obtain the overall mechanical behaviors of SPCs, such as their stiffnesses. However, the mechanical behaviors of the cable components, such as their stresses and strain, are hard to be obtained [16–19].

Therefore, it is urgent to find other methods to overcome these limitations that a test method contains. Analytical and numerical methods, which have proven effective in the oil and gas industry, provide potential solutions [20–23]. However, as SPCs increasingly deviate from conventional flexible structures through evolving configurations and escalating engineering demands, the existing analytical and numerical methods must be adapted to effectively address these more complex configurations. Thus, updating and expanding these analysis methods are necessary to manage the unique challenges presented by the advanced designs of SPCs. Due to the large amount of nonlinearity within SPCs, the numerical method has been a more potential way, especially in studying the details of the inner components.

Developing a numerical model for SPCs under tension presents two primary challenges: the selection of appropriate elements and the establishment of suitable boundary conditions. Traditionally, solid elements, which offer a high number of degrees of freedom (DOFs), are preferred for mesh generation because they capture more details, albeit at the cost of computational efficiency [24–26]. This necessitates a trade-off, particularly as the complexity of the structure increases. To address this, Bussolati [27] introduced a novel element combination that accelerates calculations for helical ropes, striking a balance between accuracy and efficiency. This method involves coupling beam elements with surface elements, allowing for the meshing of numerical helical components with fewer elements. Menard [24] adopted this approach, significantly enhancing calculation efficiency. Additionally, specialized beam elements have been developed specifically for the helical wires in flexible structures. For instance, Sævik [22] created an eight-DOF curved beam element that limits the transverse translation of helical wires, based on Kirchhoff rod theory [28,29]. This design ensures that the wire follows a loxodromic slip path.

Selecting an appropriate simulation length to mitigate boundary effects poses a significant challenge in the numerical modeling of SPCs. Chang [30] and Fang [31] have developed full-scale models to analyze the mechanical behaviors of SPCs under tension at both the overall structure and individual component levels. In these models, boundary conditions are implemented by setting both ends of the cross-sections as rigid planes, with all nodes coupled to a central reference point (RP); one RP is fully constrained, while loads are applied to the other. Fang's model [31] uses a single-core SPC, simulating the helical wires in armour layers with beam elements to enhance efficiency. Conversely, Chang's model [30] features a three-core SPC and indicates that the impact of model length on tension stiffness diminishes when the model length is near the pitch length of the outermost helical wire layer. One thing that should be noticed about this model is that the helical shapes of the inner components are disregarded, which, while improving computational efficiency, leads to deviations from actual component behavior. To sum up, existing literature generally overlooks the helical configurations of internal components in SPC models.

Incorporating helical configurations into SPC models necessitates reevaluating the appropriate model length. Currently, there is no established guidance for selecting the optimal length when configuring models this way, and excessively long models can adversely affect calculation speeds. In our previous work [32], we addressed the mechanical behavior of single-core SPCs under bending by proposing a repetitive unit cell (RUC) model. This model significantly reduces the required model length while ensuring both accuracy and efficiency in simulations. Furthermore, this model is adaptable to three-core SPCs under tension through modifications to the boundary conditions. The primary focus of our ongoing research is to enhance the RUC model for application across various SPC types, including single-core, three-core, and multi-core configurations under tension.

This paper focuses on one of the most common loads in practice, i.e., tension. The structure of this paper is organized as follows: Section 2 details the methodology for developing the proposed modeling method. Section 3 describes the necessary tests conducted to support the methodology. In Section 4, we proceed with the validation of the model. Section 5 compares the proposed model with traditional full-scale models to highlight its advantages. Section 6 presents a mechanical analysis of a three-core SPC under tension, examining both overall and component-level behaviors. Finally, Section 7 offers conclusions drawn from the study.

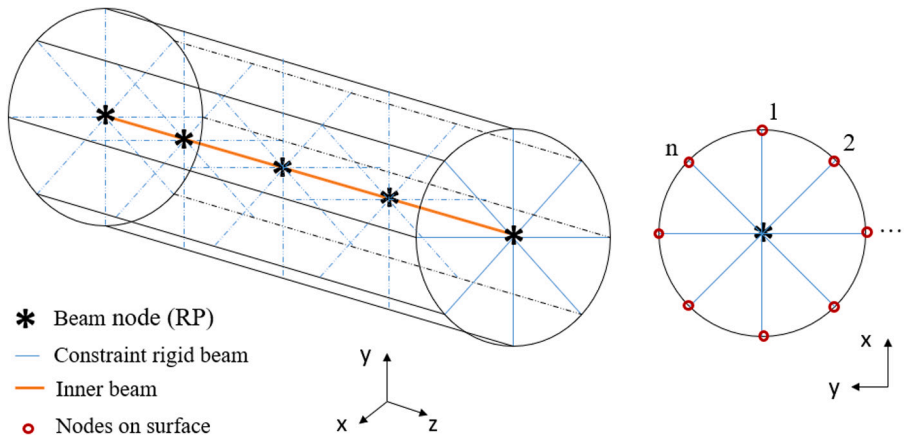

Fig. 3. The combination of beam and surface elements.

2. Methodology

The efficiency of our modeling method is enhanced through two key improvements: the selection of appropriate elements and the establishment of suitable boundary conditions. To accurately simulate the helical metals within SPCs, we employ a combination of beam and surface elements. Furthermore, we apply periodic boundary conditions to the SPCs, which effectively reduce the model length and subsequently decrease the computational resources required.

2.1. The selection of elements

The cross-section of an SPC is very complicated as it contains substantial members that need to be discrete by a huge amount of elements in FEM. Therefore, to speed up the calculation for the analysis, inspired by the work on helical ropes by Bussolati [27], a technique utilizing the combination of beam and surface elements will be used to simulate numerous helical wires and helical metals within SPCs. In this way, the number of elements in the model can be significantly reduced. The concept of the combination of helical components is illustrated in Fig. 3. As the contact issue is prominent in the analysis, surface elements are adopted to enable beam elements to capture contacts by coupling the nodes on the surface to their corresponding master nodes on a beam. Timoshenko beam elements and surface elements can be used for the beam and surface, respectively. Timoshenko beam theory offers a more accurate prediction of deformation and stress in beams than the simpler Euler–Bernoulli beam theory, making it a versatile and accurate tool for analyzing beams in situations where shear deformation and rotary inertia are significant. The surface should have neither thickness nor stiffness but be able to capture the contact among interfaces.

The reference node on the beam has translational displacement $\boldsymbol{U}$ and rotation $\boldsymbol{\phi}$, while the nodes on the surface have only the translational displacement $\boldsymbol{U}$. The relations between the RP and the corresponding nodes on the same cross-section can be described below:

$$\begin{cases} \sum_n \boldsymbol{F}^i = \boldsymbol{F}^{RP} \\ \sum_n \boldsymbol{X}^i \times \boldsymbol{F}^i = \boldsymbol{M}^{RP} + \boldsymbol{X}^{RP} \times \boldsymbol{F}^{RP} \end{cases} \tag{1}$$

where $\boldsymbol{F}$ and $\boldsymbol{M}$ are the load and moment, while $\boldsymbol{X}$ is the position of the corresponding point. i is the node sequence on the coupled cross-section, and n is the total number of nodes. The coupling approach has been proved to provide a very good compromise between accuracy and computational efficiency [27,33]. This will also be verified in Section 4 before it is applied for further analysis.

2.2. The establishment of boundary conditions

Due to the special structure configuration of the components in an SPC, periodical boundary conditions (B.C.) can be applied on both sides to eliminate the boundary effects as much as possible and speed up the calculation by reducing the model length. Periodical B.C. for beam-like structures obtained from the homogenization method can be applied to SPCs. The homogenization method on slender beam-like structures has rigorous mathematical derivation where multi-scale analysis of macroscale and microscale problems is utilized. The macroscale is in fact, an anisotropic Navier–Euler–Bernoulli–Saint-Venant beam [34], while the microscale problem is based on a unit cell. The derivation of the periodical B.C. for slender beam-like structures has been conducted a long time ago [35–37]. For the simplicity of this paper, the rigorous mathematical derivation process is not repeated again. The interested readers are recommended to find the details in [36,37]. The final equations for periodical B.C., their physical meaning and their implementation in FEM packages are given below.

Ten helical wires on a cylinder are illustrated in Fig. 4 for the convenience of the elaboration. The fundamental purpose of this method is to build a kinematic relation between the nodes on the same generatrix. The 10 wires constitute a pitch length if they are connected one by one, as shown in Fig. 5. Node A and Node B on the same generatrix are set as a couple. The corresponding A node and B node are coupled with the left master RP, denoted as C in the middle of the left cross-section, in which way the DOFs of nodes B are eliminated by the constraints while nodes A and the master RP C remain as the controlling nodes. Periodic boundary conditions have been presented by several researchers, although the equations exhibit minor differences. From the periodical boundary conditions given in [38], Node A, Node B and RP C have a relation:

$$\overrightarrow{C'B'} = \boldsymbol{R}(\boldsymbol{\phi}^C)\overrightarrow{CB} + \overrightarrow{AA'}, \quad \boldsymbol{\phi}^C = [\phi_1^C \ \phi_2^C \ \phi_3^C] \tag{2}$$

While for the periodical boundary conditions given in [39,40], Node A, Node B and RP C have a relation:

$$\overrightarrow{C'B'} = \boldsymbol{R}(\boldsymbol{\phi}^C)(\overrightarrow{CB} + \overrightarrow{AA'}), \quad \boldsymbol{\phi}^C = [\phi_1^C \ \phi_2^C \ \phi_3^C] \tag{3}$$

The original letters without a superscript denote the initial node, while the letters with the superscript represent the node after deformation. $\boldsymbol{\phi}^C$ is the rotation vector of node C and $\boldsymbol{R}(\phi^C)$ is the corresponding rotation matrix. The key difference between Eqs. (2) and (3) lies in whether the second term on the right-hand side is multiplied by the rotation matrix. Eq. (2), which is rigorously derived from the homogenization method, will be used throughout this paper. Additionally, in the case of small deformations, both equations produce almost identical

simulation results. If rotation DOFs are considered, for example, when beam elements or shell elements are utilized, then:

$$\boldsymbol{\phi}^{B} - \boldsymbol{\phi}^{A} - \boldsymbol{\phi}^{C} = 0 \tag{4}$$

In a FEM program, the matrices representing derivatives of the constraint function regarding the nodal DOFs need to be provided. Denoting the original coordinates of A, B and C as $\boldsymbol{X}^{A}$, $\boldsymbol{X}^{B}$ and $\boldsymbol{X}^{C}$, respectively, then the coordinate of A′, B′ and C′, the coordinate after deformation, can be described as $\boldsymbol{X}^{A} + \boldsymbol{U}^{A}$, $\boldsymbol{X}^{B} + \boldsymbol{U}^{B}$ and $\boldsymbol{X}^{C} + \boldsymbol{U}^{C}$, respectively. Here $\boldsymbol{U}$ is the translational displacement vector of each node. Therefore, Eq. (2) can be rewritten as:

$$\boldsymbol{X}^{\mathrm{B}} + \boldsymbol{U}^{\mathrm{B}} - \boldsymbol{X}^{C} - \boldsymbol{U}^{C} = \boldsymbol{R}(\phi^{C})(\boldsymbol{X}^{\mathrm{B}} - \boldsymbol{X}^{C}) + \boldsymbol{X}^{A} + \boldsymbol{U}^{A} - \boldsymbol{X}^{A} \tag{5}$$

Eq. (5) and Eq. (4) can be reorganized as:

$$\boldsymbol{f}_1(\boldsymbol{U}^{\mathrm{B}}, \boldsymbol{U}^{\mathrm{A}}, \boldsymbol{U}^{\mathrm{C}}) = \boldsymbol{X}^{\mathrm{B}} + \boldsymbol{U}^{\mathrm{B}} - \boldsymbol{X}^{\mathrm{C}} - \boldsymbol{U}^{\mathrm{C}} - R(\phi^{\mathrm{C}})(\boldsymbol{X}^{\mathrm{B}} - \boldsymbol{X}^{\mathrm{C}} + \boldsymbol{U}^{\mathrm{A}}) = 0 \tag{6}$$

$$\boldsymbol{f}_2(\phi^{\mathrm{B}}, \phi^{\mathrm{A}}, \phi^{\mathrm{C}}) = \boldsymbol{\phi}^{B} - \boldsymbol{\phi}^{A} - \boldsymbol{\phi}^{C} = 0 \tag{7}$$

For an FEM package to deal with the equation appropriately, the matrices representing derivatives of the constraint function with respect to the nodal DOFs need to be provided [41]. The coefficient of each matrix can be achieved by partial derivatives over the displacements of each node. It is clear that with respect to nodes A, B and C:

$$\boldsymbol{A}^{A} = \begin{bmatrix} -\boldsymbol{R}(\phi^{\mathrm{C}}) & \boldsymbol{0} \\ \boldsymbol{0} & -\boldsymbol{I} \end{bmatrix} \tag{8}$$

$$\boldsymbol{A}^{\mathrm{B}} = \boldsymbol{I} \tag{9}$$

$$\boldsymbol{A}^{C} = \begin{bmatrix} -\boldsymbol{I} & \boldsymbol{Q} \\ \boldsymbol{0} & -\boldsymbol{I} \end{bmatrix} \tag{10}$$

where $\boldsymbol{Q} = -\partial \boldsymbol{R}(\boldsymbol{\phi}^{\mathrm{C}})(\boldsymbol{X}^{\mathrm{B}} - \boldsymbol{X}^{\mathrm{C}} + \boldsymbol{U}^{\mathrm{A}})/\partial \boldsymbol{\phi}^{\mathrm{C}}$. The three matrices are 6×6 matrix when the rotation DOFs are incorporated into the model, for example, when beam element or shell elements are utilized. Otherwise, when only translational DOFs are considered, the last three rows in the three matrix can be deleted. $\boldsymbol{R}(\boldsymbol{\phi}^{C})$ has to be given in order to obtain $\boldsymbol{A}^{\mathrm{A}}$ and $\boldsymbol{A}^{\mathrm{C}}$.

An efficient and convenient way to treat finite rotations computationally, especially when there are compound rotations, is by utilizing quaternion parameters [42]. Quaternions are a mathematical concept widely used in 3D computer graphics, robotics, and physics to represent rotations and orientations. They are more numerically stable, having advantages in avoiding gimbal lock issues and providing a concise and efficient representation of 3D rotations.

Quaternion can be expressed by the combination of a scalar $q_0 \in R$ and a vector field $\boldsymbol{q} \in R^3$:

$$q = (q_0, \boldsymbol{q}) = q_0 + \boldsymbol{q} \tag{11}$$

where q_0 and $\boldsymbol{q}$ are respectively defined as:

$$\begin{cases} q_0 = \cos(\phi/2) \\ \boldsymbol{q} = \sin(\phi/2)\boldsymbol{n} \end{cases} \tag{12}$$

In terms of the four quaternion parameters q_0 and $\boldsymbol{q}$ the rotation matrix $\boldsymbol{R}$ takes the homogeneous quadratic form:

$$\boldsymbol{R} = (q_0^2 - \boldsymbol{q}^T\boldsymbol{q})\boldsymbol{I} + 2q_0\hat{\boldsymbol{q}} + 2\boldsymbol{q}\boldsymbol{q}^T \tag{13}$$

$\hat{\boldsymbol{q}}$ is the skew-symmetric matrix with axial vector $\boldsymbol{q}$. The corresponding component representation is:

$$R_{ij} = (q_0^2 - q_k q_k)\delta_{ij} - 2\epsilon_{ijk}q_0 q_k + 2q_i q_j \tag{14}$$

In full matrix form, the rotation representation is:

$$\boldsymbol{R} = \begin{bmatrix} r_0^2 + r_1^2 - r_2^2 - r_3^2 & 2(r_1r_2 - r_0r_3) & 2(r_1r_3 + r_0r_2) \\ 2(r_1r_2 + r_0r_3) & r_0^2 - r_1^2 + r_2^2 - r_3^2 & 2(r_2r_3 - r_0r_1) \\ 2(r_1r_3 - r_0r_2) & 2(r_2r_3 + r_0r_1) & r_0^2 - r_1^2 - r_2^2 + r_3^2 \end{bmatrix} \tag{15}$$

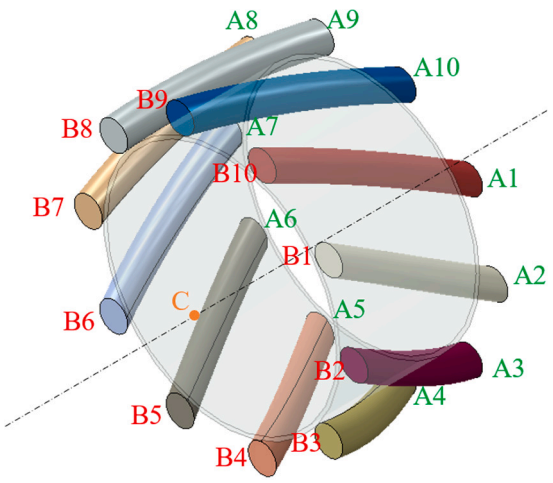

Fig. 4. Nodes involved in periodicity conditions on the helical wire layer.

The coefficients in Eqs. (8) and (10) can thus be obtained.

As this model is proposed to deal with not only single-core SPCs but also three-core SPCs and other multi-core SPCs, the rules for selecting the model length regarding these different types of SPCs should be unified. The requirement of the model length is:

$$l = k\frac{p_i}{m_i} \tag{16}$$

where $k \in \mathbb{N}$, p is the pitch length, m is the number of helixes, and the index i is the sequence of the current layer. For a single-core SPC, the helical components only exist in the armour layers, and the inner components are all straight. Therefore, the model length is only determined by the pitch lengths and the number of wires in the armour layers. However, when it comes to a multi-core SPC, the inner components are also helical and will also yield a model length based on Eq. (16). The ultimate model length will be the maximum value from the lengths regarding not only armour layers but also the inner helical components. Typically, the value is determined by the inner helical components because its m, i.e., the number of helical components, is very small. For example, $m = 3$ in a three-core SPC regarding the inner helical components.

The solution to the periodical boundary conditions is similar to three-body movements [43] with specific internal constraints, which will cause rigid body displacements. Therefore, extra constraints on the structure are needed to eliminate the effect of the rigid body displacements. Unlike the approach employed by Tyrberg [25], where a viscous damping coefficient is added to the model that requires a ratio of damping energy to total strain energy less than 5% at the end of the simulation, another B.C. is proposed in this paper to get rid of the damping effect from the rigid body movement. This B.C. is unified and can be conveniently applied to single-core and multi-core SPCs. More importantly, the setup of the B.C. is capable of dealing with not only pure loadings such as tension or bending but also combined loading cases conveniently. The unified B.C. for a single-core SPC and a three-core SPC is illustrated in Fig. 6.

The outer PE cylinder on both sides is coupled with an RP in the middle of its corresponding cross-section. The other components on both sides are constricted by the periodical boundary conditions. The right RP is fixed, while a tension force T is applied on the left RP. The primary goal of introducing the coupling was to eliminate rigid body movements while minimizing the effects from the coupling as much as possible. Given the small thickness and low Young's modulus of the outermost PE layer, the boundary effects induced by coupling the outermost PE layer is negligible. This will be verified by comparing the simulation results with the test data presented below. As this model

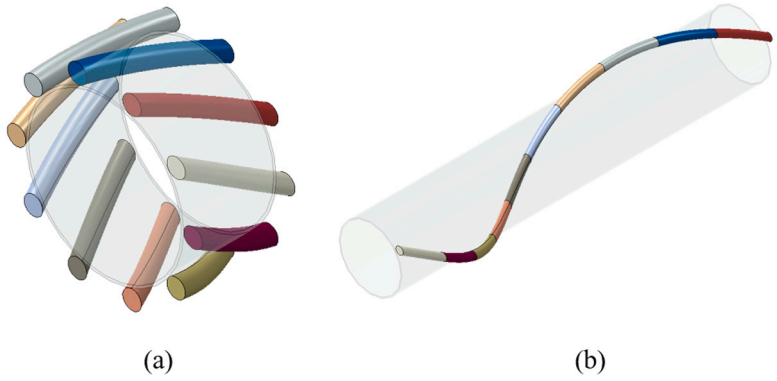

Fig. 5. The wires involving periodical boundary conditions (a) and their corresponding location in one pitch (b).

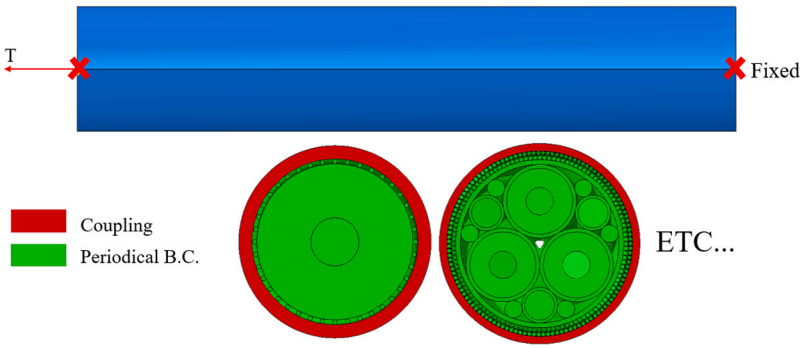

Fig. 6. The illustration of the boundary conditions for SPCs under combined loadings.

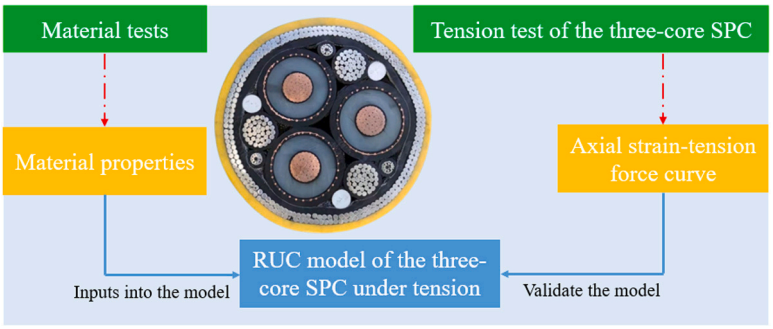

Fig. 7. The calibration and validation flow chart.

is based on the periodical boundary conditions on a repetitive unit cell (RUC), for the convenience of the elaboration in the following content, this proposed model will be termed RUC model.

3. Tests

The core of this part is the validation of the RUC model under tension, which is accomplished after obtaining the data from the material test and the tension test regarding a three-core SPC. Fig. 7 shows clearly how the tests work during the validation process. Material tests provide necessary material properties for the construction of the RUC models. Finally, the axial strain-tension force curve from the tension test regarding the three-core SPC will be used to validate the RUC model.

3.1. Material tests

The test samples in this paper are 35 kV alternative current dynamic power cables produced by Oriental Cable (NBO). The nomination of the main components within the cable is shown in Fig. 8.

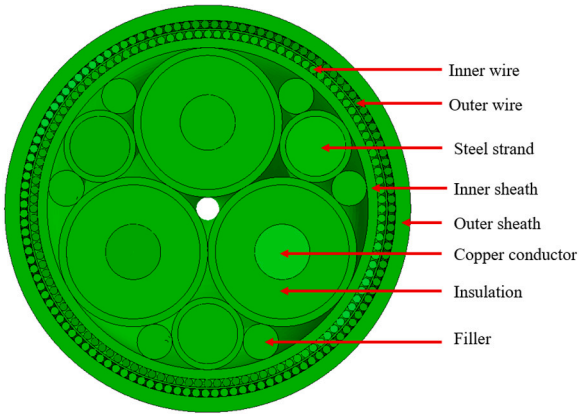

Fig. 8. The nomination of the main components.

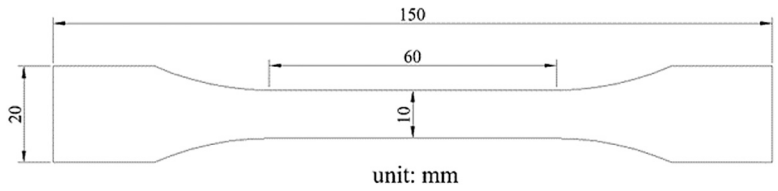

Fig. 9. The detailed dimensions of MDPE & XLPE.

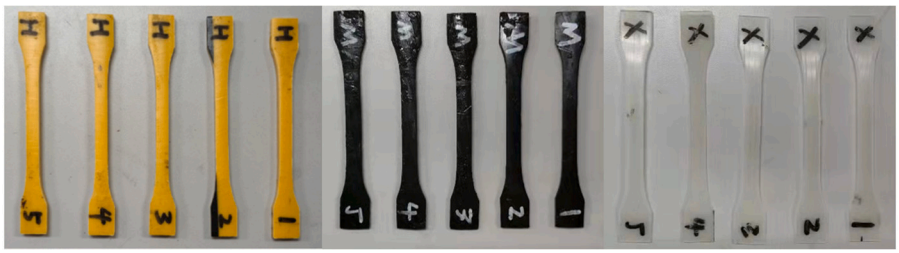

Fig. 10. Dumbbell shape of HDPE (left), MDPE (middle) & XLPE (right).

Fig. 11. Tension test under an electronic universal testing machine.

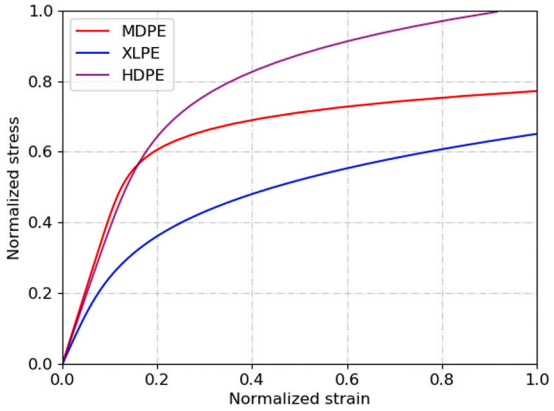

Fig. 12. Normalized strain vs. stress curves for MDPE, XLPE & HDPE.

The detailed geometry and material parameters are not given for commercial reasons, and the data in the following content are normalized. Material polyethene (PE) tends to change its behavior after being extruded into cylinder shapes. There are three types of PE in the SPC sample: HDPE, XLPE and MDPE. Therefore, material tests are performed first to obtain the stress–strain relations of the PE.

According to ISO 527-2012 [44], PE cut from cable samples was made into dumb-bell shapes with a dimension in Fig. 9. All three types of PE have five samples, as shown in Fig. 10. The strains during the tension process were recorded by extensometers on an electronic universal test machine, as shown in Fig. 11. The test machine has a measuring range of 2.5 KN, and the tension speed was controlled at 5 mm/min for all the samples.

After the test, the stress and strain relation of each sample can be obtained. The stress–strain relations can be obtained through the linear interpolation method and averaging process of the five samples of each material. The true stress and true strain are calculated according to:

$$\varepsilon_{True} = \ln(1 + \varepsilon_{Nominal}) \tag{17}$$

$$\sigma_{True} = \sigma_{Nominal}(1 + \varepsilon_{Nominal}) \tag{18}$$

To facilitate the manipulation in the numerical model, an expression for the true stress–strain relationship is generated via the Ramberg–Osgood equation [45]. The total strain is the sum of the elastic strain and the plastic strain, which results in:

$$\varepsilon_t = \varepsilon_e + \varepsilon_p = \frac{\sigma}{E} + (\frac{\sigma}{K})^g \tag{19}$$

where σ is the stress, K the nonlinear modulus, g the hardening exponent, E the Young's modulus calculated as the secant modulus when the true strain is between 0.05% and 0.25% based on the standard ISO527-2012 [44]. The generated Ramberg–Osgood curves of the three types of PE after normalization are shown in Fig. 12.

3.2. Tension test

The dimension of the test cable is given in Fig. 13. The total length of the cable sample is 9 m. Two bend stiffeners are installed on both sides through which the loadings are applied, which makes the valid length of the sample 7 m. The bend stiffener is used to clamp the cable tightly so that it does not slip away from the loading device. During the tension test, one of the bend stiffeners is totally fixed, while the other one is able to rotate and is pulled through an axial force. The test configuration is shown in Fig. 14.

To prepare the cable samples for testing, a preliminary tension of 70 kN was applied for approximately 10 min to straighten the cable, which was suspended between two end fittings. This initial elongation

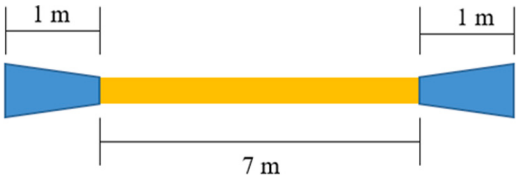

Fig. 13. A sketch of the tension test.

Fig. 14. Tension test facility.

is not included in the test results. Subsequently, the load was gradually increased from 70 kN to 220 kN in 20 kN increments at a low speed to minimize dynamic effects. To establish a stable tension behavior, this tension cycle–ranging from 70 kN to 220 kN and back to 70 kN–was repeated several times. An axial displacement sensor was installed directly on the cable end, rather than on the bend stiffener, to ensure accurate measurement and avoid any slippage. Additionally, to reduce the impact of gravity on the measurements, the cable was suspended using a wide rope. Data from the installed displacement and loading sensors were used to determine the relationship between axial strain and axial force.

4. Validation of the RUC model under tension

In this part, the axial strain-tension force curve is used to validate the RUC model of the three-core SPC under tension. Firstly, the construction of the three-core SPC is introduced, where the reliability of the beam plus surface element will be verified under the tension case. Then, the validation of the RUC model against the test result is presented.

The model is constructed in the FEM software package ABAQUS/Standard [46]. ABAQUS is a powerful finite element analysis (FEA) software suite widely used in engineering and simulation. Developed by SIMULIA, part of Dassault Systèmes, ABAQUS provides a comprehensive platform for simulating and analyzing complex physical behavior of structures, components, and materials.

Due to the complex geometries of SPC samples, certain simplifications and assumptions are necessary to strike a balance between accuracy and efficiency in our simulations. Engineers interested in conducting more detailed investigations of specific layers have the flexibility to incorporate them into their models, building upon the existing modeling techniques.

1. The extremely thin layers compared with other layers are combined with the neighboring layers, as they will introduce a large calculation cost, but their contribution can be ignored.

2. The copper conductors and steel strands in the cable product comprise numerous helical wires. However, they are simplified into a solid cylinder with an equivalent cross-section area. This assumption is satisfied when an SPC is under small deformation.

3. The initial deformation of the cross-section of the SPC sample is ignored, and the model is built according to the geometry information in the specification provided by the cable manufacturer.

The geometries of the three-core SPC model are presented in Fig. 15. Its length is calculated according to Eq. (16), and its boundary conditions are set according to those in Section 2.2. The RUC model for the three-core SPC is 792 mm.

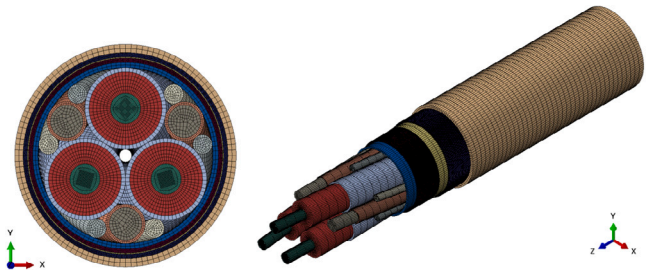

Fig. 15. The RUC model of the three-core SPC.

All the contact interactions among each component are taken into account. Surface-to-surface discretization method is used to model the contact between surfaces where both the tangential behavior and normal behavior employ the penalty method. The friction coefficient provided by the cable manufacturer is 0.3. The normal contact is set as the default hard contact.

Before the validation, the soundness of the beam plus surface elements needs to be verified. For the three-core SPC, since the inner components, as shown in Fig. 15, are helix with periodical patterns, the influence of the helical configurations is also taken into account. After this consideration, the model length becomes larger, and there are much more helical wires in the three-core SPC, resulting in cumbersome and time-consuming calculations. Therefore, the technique of beam plus surface elements will be used.

Beam plus surface elements are used to simulate numerous helical wires and helical metals within the three-core SPC, including the steel strand, copper conductor, inner wire and outer wire shown in Fig. 8. It was mentioned that the coupling approach had been proven to provide a very good compromise between accuracy and computational efficiency [27,33]. The model built with all solid elements is termed Case-1, while the other one built with beam plus surface elements is termed Case-2. The boundary conditions of both models under tension have been given in Section 2.2 in Fig. 6. The right side is totally fixed, and a tension force is applied to the left RP. The left RP is allowed to rotate, like the situation in the tension test.

The mesh results of the three-core SPC in these two ways are shown in Figs. 16 and 17. The mesh densities in the axial direction for both models are the same. All the mesh details for the solid elements in both models are the same as well, in addition to the helical metals.

The information of both models is listed in Table 1 for reference. The number of elements and nodes decreases from 3150320 in Case-1 to 1588208 in Case-2. All models were run on the DelftBlue Linux supercomputer [47] with 16 cores. The calculation time of Case-1 is found to decrease from 70.3 h to 3.7 h, with around 19 times more efficient than Case-2. The soundness of the beam plus solid technique is verified by comparing the axial strain-tension force curve from both models, as shown in Fig. 18. The curve predicted by the solid element is a straight line, while the one given by the beam plus surface elements is a bit bendy, which is caused by the difference in the element property in models. To be specific, unlike solid elements, the surface elements do not have deformation in the radial direction [46]. Although the surface elements are still able to capture the contact force and enable its propagation, this distinction in element property leads to curves with minor different styles. However, the difference regarding the stiffnesses from both models after curve fitting is 0, illustrating the soundness of the simplification. Therefore, for the consideration of the model efficiency, the following analysis will rely on the model built with the technique of beam plus surface.

Subsequently, the simulation result by Case-2 is validated by the test results on the normalized strain-normalized tension force curve, as shown in Fig. 18. It is found that the curves basically align with each other. The tension stiffness from the test is normalized to 1, and the

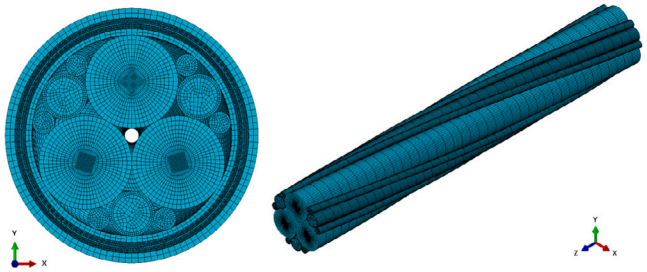

Fig. 16. Mesh of the three-core SPC by using solid elements.

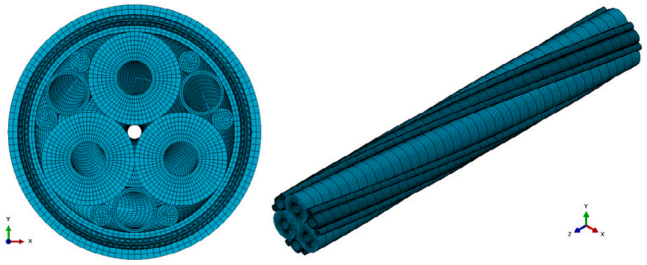

Fig. 17. Mesh of the three-core SPC by using beam & surface helical wires.

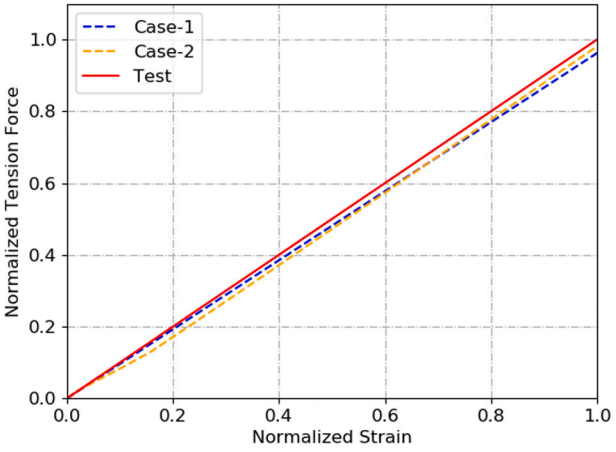

Fig. 18. The axial strain-tension force curves from the two RUC models.

stiffnesses from both cases are given in Table 1. In fact, the stiffnesses from Case-2 and test after curve fitting have an error of only 4.0%, illustrating the reliability of the RUC model.

5. Full-scale model

To verify the effectiveness of the RUC model over traditionally-built numerical models from the perspectives of accuracy and efficiency, a full-scale model is built for the comparison. The full-scale model here refers to the numerical model that is not based on periodical boundary conditions. The length of the full-scale model cannot be reduced by taking advantage of the helical configurations of the components, which makes its length longer. The details are given below.

The mesh density of the full-scale model has been the same as that of the RUC model. The length selected here is 2376 mm, one pitch length of the inner components. As shown in Fig. 19, both ends of the full-scale models are coupled to an RP, respectively. One of the RPs is totally fixed, whereas on the other RP, U1, U2, U4 as well as U5 are locked and tension is applied in the axial direction. The information of the full-scale model together with the RUC model for tension case are

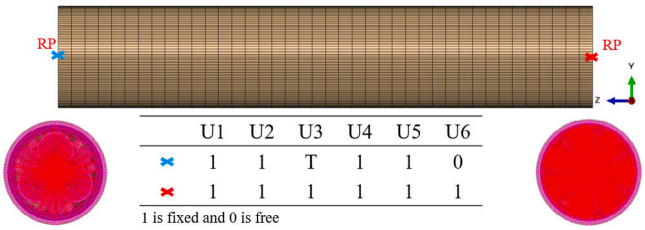

Fig. 19. The boundary conditions of the full-scale model under tension.

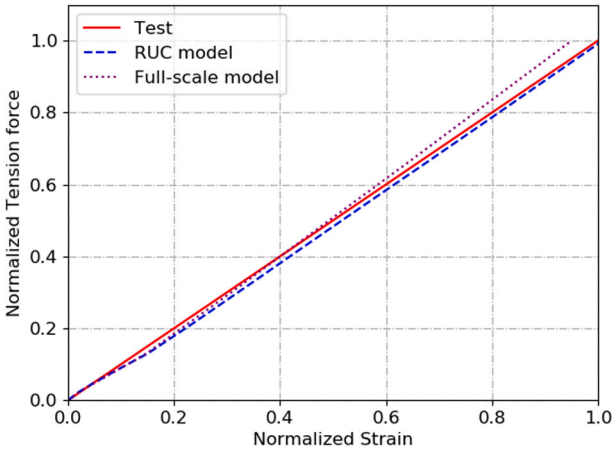

Fig. 20. The strain-tension force curves from the RUC model and three full-scale models.

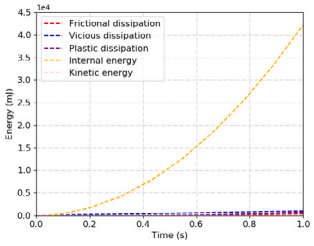

Fig. 21. The variation of the plasticity dissipation and the internal energy throughout the tension based on RUC model.

Table 1
The information of the two types of RUC model under tension.

	Case-1	Case-2
Element types	Solid	Solid & beam & surface
Number of elements	3 150 320	1 588 208
Number of nodes	6 276 347	2 905 591
Tension stiffness	0.96	0.96
Cost time	70.3 h	3.7 h

given in Table 2. Their results will be discussed together with the RUC model, as well as the test results in the next section.

6. Results and discussions

The RUC model under tension has been validated by the test results. Then, the mechanical behavior of the components can be studied based on this model at the overall and component levels.

6.1. Cable overall behavior

The axial strain-tension force curve from the full-scale model is put together with the RUC and the test results, as shown in Fig. 20. The

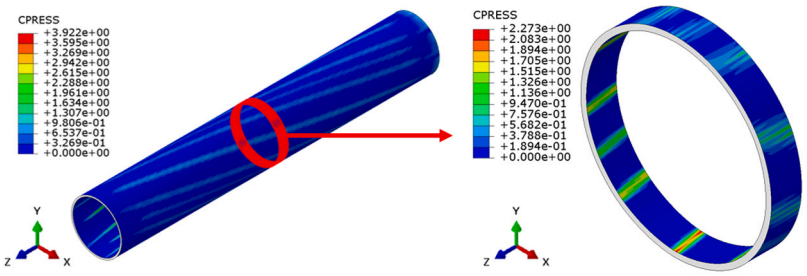

a. Contact pressure along the inner sheath b. Contact pressure of the middle section

Fig. 22. The contact pressure (Unit: MPa) of the inner sheath within the cable under tension when t = 1 s.

Table 2
The information of the RUC model and the full-scale model under tension.

	Full-scale model	RUC model
Length	2376 mm	792 mm
Number of elements	4 745 288	1 588 208
Number of nodes	8 642 538	2 901 751
Tension stiffness	1.06	0.96
Cost time	22.4 h	3.5 h

tension stiffness predicted by the full-scale model is larger than that of the test results, with an error of 6.0%, which might be caused by the boundary effect that can be eliminated much more if the full-scale model is prolonged longer. However, the longer the model is, the more calculation resources it will cost. Notice, the coupling of the outer PE in the RUC model can also introduce some boundary effect, which affects the accuracy of the results. Considering the error between the RUC model and the test is only 4.0%, the affects from the boundary effect are within the acceptable level and the RUC model outperforms the full-scale model from the perspective of accuracy. Besides, the calculation time of the full-scale models and the RUC model are summarized in Table 2. It is found that the RUC model is almost 7 times faster than the full-scale model, illustrating its efficiency.

The energy dissipation during the tension case is of interest, so five types of energy variation, frictional dissipation, vicious dissipation, plastic dissipation, internal energy and kinetic energy, throughout the simulation process from the RUC model are outputted and presented in Fig. 21. The time here does not have any physical meaning but only represents a loading process for the convenience of explanation. The tension force is applied linearly to a maximum value when t equals 1 s. First, it is found that the kinetic energy is near 0, illustrating that the dynamic effect can be safely ignored during the simulation. Second, the contribution from the frictional dissipation and viscous dissipation are not so large during the tension process, which demonstrates that slippage is not substantial in the system. Also, the plastic dissipation can be ignored. This will be further studied through the Mises stress distribution in the next subsection at the component level.

6.2. Cable component behavior

When zooming into the component level, firstly, the contact pressure on the inner sheath within the cable under tension is extracted and given in Fig. 22. Again, the time here does not have any physical meaning but only represents that the tension force is applied linearly to a maximum value when t equals 1 s. It is found that the maximum contact stresses are located at the contact areas between the inner sheath and the neighboring internal components. To investigate how the contact pressure distributes around the cross-section of the inner sheath, a middle section is cut out, as shown in Fig. 22b. Then the contact pressure of the inner sheath at this cross-section when t = 0.5 s and t = 1 s is outputted and shown in Fig. 23.

It can be found that the maximum contact pressure appears at the contact point between the inner sheath and the inner components,

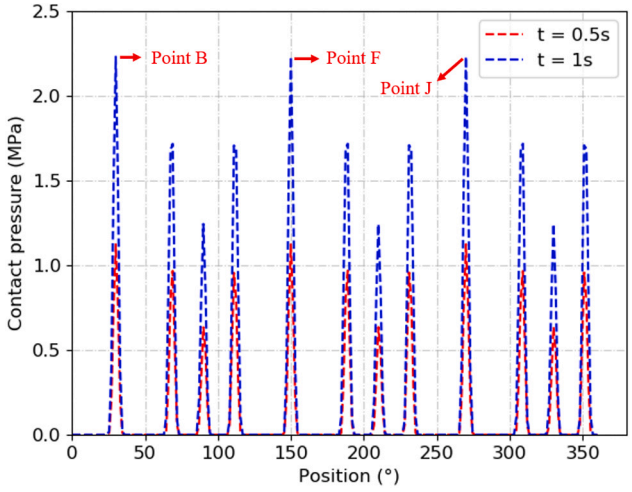

Fig. 23. Contact pressure of the inner sheath under tension.

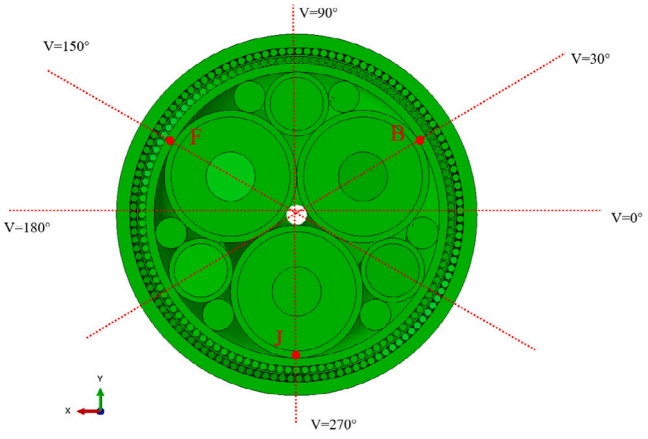

Fig. 24. Illustration of the nodes in the middle cross-section of the three-core SPC.

while the areas with no contact do not have any pressure. The maximum contact pressure appears at the contact point between the inner sheath and the three cores, namely Point B, Point F and Point J, corresponding to the nodes in Fig. 24. The values on the three points are almost the same in the tension case.

One also needs to check the stress distribution of the components for the tension case, as shown in Fig. 25a. It can be found that the metals in the SPC, including the steel strand, helical wires and conductors, bear much of the stresses. As Young's modulus of the material steel is much higher than that of the material copper, the stress of the former is also much higher than that of the latter. All the metals are within their elastic phase. Most PE materials are also within their elastic phase with

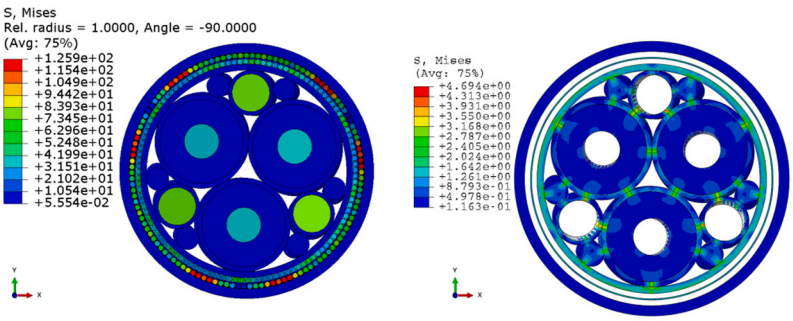

a. All the components in the middle cross section b. All the PE material in the middle cross section

Fig. 25. The Mises stress distribution (Unit: MPa) of the cable under tension when t = 1 s.

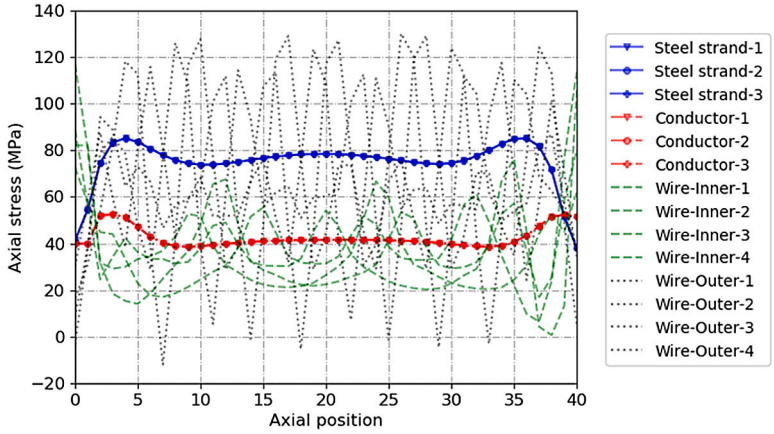

Fig. 26. Axial stress of the metals when t = 1 s in the tension case.

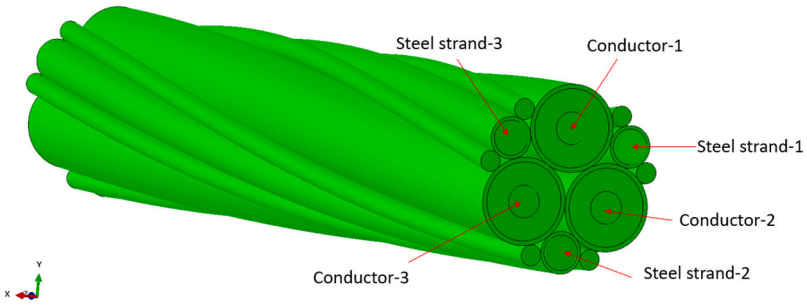

Fig. 27. Illustration of all the inner metals.

only a few parts along the boundary entering into the plasticity, which does not have a large influence on the overall tension behavior and thus, in the simulation, their plasticity can also be disregarded for the calculation efficiency. It is observed from Fig. 25b that the insulation layers bear quite small stress, which increases the safety of the overall SPC as the insulation layer should be protected in real life to get rid of water tree or electrical tree that are highly related to high-stress distribution.

The stress distributions of the metals along the axial direction need to be extracted for further analysis. First, the nomination of the three steel strands and three copper conductors are illustrated in Fig. 27. As there are numerous helical wires in two armour layers, and the axial stresses of these wires are distributed unevenly due to the uneven pressure, only four wires in each layer are taken out for illustration purpose. Their starting positions correspond to $V = 0°$, $V = 90°$, $V = 180°$ and $V = 270°$ in Fig. 24. The axial stress distributions of these metals are then shown in Fig. 26.

From Fig. 26, it is found that the helical wires in both armour layers bear more stress than the inner metals. The inner metals only bear tension without any compression stress. The axial stresses of the three steel strands along the axial position are basically the same, thus the curves of the three steel strands are overlapped. This is the same for the conductors. The stresses near the boundaries are abnormal due to the boundary effect. If one wants to get rid of this effect, then it is suggested to double the length of the RUC model and only output the results in the middle. However, this will cause a huge increase in the calculation; thus, whether it is necessary to take this step depends on the requirement of practical engineering and the calculation resources. The steel strands bear nearly two times the stress as the conductors, which reduces the possibility of fatigue for conductors by avoiding excessive stress. Besides, it can be observed that the axial stress borne by the outer armour layer is much larger than that by the inner armour layer.

7. Conclusions

In this paper, an effective modeling method is proposed to deal with the mechanical analysis of SPCs. As the model from the modeling method is based on a repetitive unit cell (RUC), it is termed as RUC model. A tension test regarding a three-core SPC is presented. The obtained tension stiffness is used to validate the RUC model under tension. The RUC model is 4.0% smaller than the test results regarding the tension stiffness, while the full-scale model is 6% larger than the test results. Besides, the RUC model is around 7 times more efficient than the traditionally built full-scale model we have simplified. Therefore, the developed RUC model holds the potential for conducting tension studies on SPCs with a good balance between accuracy and efficiency. Then, the local mechanical behaviors of the three-core SPC under tension are studied in detail through the RUC model at the overall and component levels. The key findings of this paper can be summarized as follows:

(1) Stick–slip Absence: In cases of SPCs under tension, there is no significant stick–slip problem, aligning with the RUC model's findings where both friction and viscous dissipation are negligible.

(2) Material Behavior: Under the conditions of small deformation during tension simulations, plastic deformation can be disregarded, and the materials can be considered to exhibit linear elasticity. This assumption does not significantly impact the simulation outcomes.

(3) Pressure Distribution: The internal arrangement of helical components leads to uneven pressure distribution on the inner sheath, resulting in uneven stress across the wires of the armour layers. This highlights the inaccuracies that can arise from assuming evenly distributed pressure in analytical methods.

(4) Stress Distribution: Metals, particularly helical wires, bear the majority of the stress, with wires in the outer armour layer experiencing greater stress than those in the inner layer.

Additionally, an SPC is subjected not only to tension but also to bending, and often to a combination of both in practical applications. It is crucial to validate the RUC model under bending as well. Future studies will include local mechanical analysis of SPCs under these combined stresses to enhance design accuracy, which we will address in our subsequent work.

CRediT authorship contribution statement

Pan Fang: Writing – review & editing, Writing – original draft, Visualization, Validation, Software, Methodology, Investigation, Formal analysis, Data curation, Conceptualization. **Xiao Li:** Writing – review & editing, Investigation. **Xiaoli Jiang:** Supervision, Resources, Project administration, Investigation. **Hans Hopman:** Supervision, Project administration. **Yong Bai:** Supervision, Project administration.

Declaration of competing interest

The authors declare the following financial interests/personal relationships which may be considered as potential competing interests: Pan Fang reports financial support was provided by China Scholarship Council [grant number 201906320047]

Data availability

The data that has been used is confidential.

Acknowledgment

The first author would like to express gratitude for the support from the China Scholarship Council [grant number 201906320047] and Orient Cable (NBO) in providing the test samples.

References

[1] Worzyk T. Submarine power cables: design, installation, repair, environmental aspects. Springer Science & Business Media; 2009.
[2] Trust C. Floating wind joint industry project – phase 2 summary report. 2022, URL https://www.carbontrust.com/our-work-and-impact/impact-stories/floating-wind-joint-industry-programme-jip/floating-wind-jip-phase-ii.
[3] Young D, Ng C, Oterkus S, Li Q, Johanning L. Assessing the mechanical stresses of dynamic cables for floating offshore wind applications. J Phys: Conf Ser 2018;1102:012016.
[4] Rentschler MU, Adam F, Chainho P. Design optimization of dynamic inter-array cable systems for floating offshore wind turbines. Renew Sustain Energy Rev 2019;111:622–35.
[5] Conseil international des grands réseaux électriques Comité d'études B1. Recommendations for mechanical testing of submarine cables. CIGRÉ; 2015.
[6] DNVGL. Subsea power cables for wind power plants. 2020, URL https://www.dnv.com/energy/standards-guidelines/dnv-st-0359-subsea-power-cables-for-wind-power-plants.html.
[7] Ikhennicheu M, Lynch M, Doole S, Borisade F, Wendt F, Schwarzkopf M-A, et al. Review of the state of the art of dynamic cable system design. Brussels, Belgium: COREWIND; 2020.
[8] WIND EUROPE. The EU offshore renewable energy strategy. 2020, URL https://windeurope.org/policy/position-papers/the-eu-offshore-renewable-energy-strategy/.
[9] TRUST, CARBON. Floating wind joint industry programme – phase IV summary report. 2022, URL https://www.carbontrust.com/our-work-and-impact/impact-stories/floating-wind-joint-industry-programme-jip/floating-wind-jip-phase-iv.
[10] ETIPWind, Roadmap. Roadmap. 2019, URL https://etipwind.eu/roadmap/.
[11] CIGRE TB 610. CIGRE TB 610 - offshore generation cable connections. 2015, URL https://www.researchgate.net/publication/338388640_CIGRE_TB_610_-_Offshore_generation_cable_connections/citations.
[12] NEXANS. Subsea cables – mv medium voltage power & fibre optics cables. 2019, URL https://www.powerandcables.com/subsea-cables-joints-terminations/.
[13] Baker Hughes. Power generation. 2020, URL https://www.plasteurope.com/news/SAUDI_ARAMCO_t245063/.
[14] DNV-RP-F401. Electrical power cables in subsea applications. 2022, URL https://www.dnv.com/oilgas/download/dnv-rp-f401-electrical-power-cables-in-subsea-applications.htm.
[15] RILEY C, et al. Hv cable qualifications to iec 62067-2006 and icea s-108-720-2004. In: Jicable conf. 2011.
[16] Poon CT, Mullins C, Radziunas L, O'Connell E, Connolly A, Leen S. Finite element design study of dynamics in submarine power cables for offshore renewable wind energy. In: International conference on offshore mechanics and arctic engineering. Vol. 86618, American Society of Mechanical Engineers; 2022, V001T01A023.
[17] 2H Offshore. Subsea cable failures: What we know and what we don't. 2022, URL https://ore.catapult.org.uk/wp-content/uploads/2022/10/Dynamic-Cable-Technology-Qualification-Oct-2022.pdf.
[18] Thai H-T, Kim S-E. Nonlinear static and dynamic analysis of cable structures. Finite Elem Anal Des 2011;47(3):237–46.
[19] Nicholls-Lee R, Thies PR, Johanning L. Coupled modelling for dynamic submarine power cables: interface sensitivity analysis of global response and local structural engineering models. 2021.
[20] Sævik S. Theoretical and experimental studies of stresses in flexible pipes. Comput Struct 2011;89(23–24):2273–91.
[21] Knapp R. Derivation of a new stiffness matrix for helically armoured cables considering tension and torsion. Internat J Numer Methods Engrg 1979;14(4):515–29.
[22] Sævik S. A finite element model for predicting stresses and slip in flexible pipe armouring tendons. Comput Struct 1993;46(2):219–30.
[23] Bai Y, Liu T, Ruan W, Chen W. Mechanical behavior of metallic strip flexible pipe subjected to tension. Compos Struct 2017;170:1–10.
[24] Ménard F, Cartraud P. A computationally efficient finite element model for the analysis of the non-linear bending behaviour of a dynamic submarine power cable. Mar Struct 2023;91:103465.
[25] Tjahjanto DD, Tyrberg A, Mullins J. Bending mechanics of cable cores and fillers in a dynamic submarine cable. In: International conference on offshore mechanics and arctic engineering. Vol. 57694, American Society of Mechanical Engineers; 2017, V05AT04A038.
[26] Leroy J-M, Poirette Y, Brusselle Dupend N, Caleyron F. Assessing mechanical stresses in dynamic power cables for floating offshore wind farms. In: International conference on offshore mechanics and arctic engineering. Vol. 57786, American Society of Mechanical Engineers; 2017, V010T09A050.
[27] Bussolati F. Modèle multi-échelle de la fatigue des lignes d'ancrage câblées pour l'éolien offshore flottant (Ph.D. thesis), Université Paris-Saclay (ComUE); 2019.
[28] Love, Augustus Edward Hough. A treatise on the mathematical theory of elasticity. University Press; 1927.
[29] Kirchhoff G. Über das gleichgewicht und die bewegung eines unendlich dünnen stabes. J Math 1858;291.

[30] Chang H-C, Chen B-F. Mechanical behavior of submarine cable under coupled tension, torsion and compressive loads. Ocean Eng 2019;189:106272.
[31] Fang P, Jiang X, Hopman H, Bai Y. Mechanical responses of submarine power cables subject to axisymmetric loadings. Ocean Eng 2021;239:109847.
[32] Fang P, Li X, Jiang X, Hopman H, Bai Y. Bending study of submarine power cables based on a repeated unit cell model. Eng Struct 2023;293:116606.
[33] Ménard F, Cartraud P. Solid and 3D beam finite element models for the non-linear elastic analysis of helical strands within a computational homogenization framework. Comput Struct 2021;257:106675.
[34] Cartraud P, Messager T. Computational homogenization of periodic beam-like structures. Int J Solids Struct 2006;43(3–4):686–96.
[35] Kolpakov A. Calculation of the characteristics of thin elastic rods with a periodic structure. J Appl Math Mech 1991;55(3):358–65.
[36] Buannic N, Cartraud P. Higher-order effective modeling of periodic heterogeneous beams. I. Asymptotic expansion method. Int J Solids Struct 2001;38(40–41):7139–61.
[37] Buannic N, Cartraud P. Higher-order effective modeling of periodic heterogeneous beams. II. Derivation of the proper boundary conditions for the interior asymptotic solution. Int J Solids Struct 2001;38(40–41):7163–80.
[38] Rahmati M, Bahai H, Alfano G. An accurate and computationally efficient small-scale nonlinear FEA of flexible risers. Ocean Eng 2016;121:382–91.
[39] Lukassen TV, Gunnarsson E, Krenk S, Glejbøl K, Lyckegaard A, Berggreen C. Tension-bending analysis of flexible pipe by a repeated unit cell finite element model. Mar Struct 2019;64:401–20.
[40] Smith DM, Cunningham LS, Chen L. Efficient finite element modelling of helical strand cables utilising periodicity. Int J Mech Sci 2023;108792.
[41] Diehl T. Formulation of a user MPC to simulate beam-type transport problems. Tech. rep., MFSP Internal Report, Department of Mechanical Engineering, University of . . . ; 1993.
[42] Krenk S. Non-linear modeling and analysis of solids and structures. Cambridge University Press; 2009.
[43] Strogatz SH. Nonlinear dynamics and chaos with student solutions manual: With applications to physics, biology, chemistry, and engineering. CRC Press; 2018.
[44] ISO B, et al. Plastics–determination of tensile properties. British Standard, Germany; 1997.
[45] Ramberg W, Osgood WR. Description of stress-strain curves by three parameters. Tech. rep., 1943.
[46] Abaqus V. Documentation. Dassault Systemes Simulia Corporation. 2014. 6.14. 651: 6.2. Belytschko T. & Black T. Elastic crack growth in finite elements with minimal remeshing. Int J Numer Methods Eng 1999;45(5):601–20.
[47] DELFTBLUE. Delft high performance computing centre (dhpc), delft- blue supercomputer (phase 1). 2022, URL https://www.tudelft.nl/dhpc/ark/delftbluephase1.